

Gravity Spectra from the Density Distribution of Earth's Uppermost 435 km

Josef Sebera¹ · Roger Haagmans² · Rune Floberghagen¹ ·
Jörg Ebbing³

Received: 11 July 2017 / Accepted: 21 October 2017 / Published online: 6 November 2017
© Springer Science+Business Media B.V. 2017

Abstract The Earth masses reside in a near-hydrostatic equilibrium, while the deviations are, for example, manifested in the geoid, which is nowadays well determined by satellite gravimetry. Recent progress in estimating the density distribution of the Earth allows us to examine individual Earth layers and to directly see how the sum approaches the observed anomalous gravitational field. This study evaluates contributions from the crust and the upper mantle taken from the LITHO1.0 model and quantifies the gravitational spectra of the density structure to the depth of 435 km. This is done without isostatic adjustments to see what can be revealed with models like LITHO1.0 alone. At the resolution of 290 km (spherical harmonic degree 70), the crustal contribution starts to dominate over the upper mantle and at about 150 km (degree 130) the upper mantle contribution is nearly negligible. At the spatial resolution < 150 km, the spectra behavior is driven by the crust, the mantle lid and the asthenosphere. The LITHO1.0 model was furthermore referenced by adding deeper Earth layers from ak135, and the gravity signal of the merged model was then compared with the observed satellite-only model GOCO05s. The largest differences are found over the tectonothermal cold and old (such as cratonic), and over warm and young areas (such as oceanic ridges). The misfit encountered comes from the mantle lid where a velocity–density relation helped to reduce the RMS error by 40%. Global residuals are also provided in terms of the gravitational gradients as they provide better spatial localization than gravity, and there is strong observational support from ESA's satellite gradiometry mission GOCE down to the spatial resolution of 80–90 km.

Keywords Density distribution model · Satellite Gravimetry · Lithosphere · Upper mantle · GOCE · Gravitational gradients

✉ Josef Sebera
josef.sebera@esa.int

¹ ESA/ESRIN, Largo Galileo Galilei 1, Casella Postale 64, 00044 Frascati (Roma), Italy

² ESA/ESTEC, Postbus 299, 2200 AG Noordwijk, The Netherlands

³ Christian-Albrechts-Universität zu Kiel, Christian-Albrechts-Platz 4, 24118 Kiel, Germany

1 Introduction

The balance between the gravitational and internal pressure force dominantly governs how celestial bodies are structured (Bertotti et al. 2012). Soon after the launch of the first artificial satellite, a misfit of about 0.5% was found between the hydrostatic (theoretical) flattening (1/299.9) and the value obtained from orbit perturbations (1/298.3), see, e.g., (James and Kopal 1962; Denis et al. 1997). The hydrostatic equilibrium (as well as the deviation from it) in the Earth is not exclusively reserved for a single frequency such as J_2 . At the resolution of few thousands of kilometers, the hydrostatic equilibrium is affected by the convective flows in the mantle (Anderson 2007) where the dominant geoid patterns are produced (Chase 1979; Hager et al. 1985). Over wavelengths down to about 100 km (Turcotte and Schubert 2002), the hydrostatic equilibrium is characterized by means of isostasy. At smaller scales, a compensating mechanism is less profound because the lithosphere becomes rigid enough to bear the topography; hence the (high-frequency) free air gravity anomalies do correlate with the topography (De Pater and Lissauer 2015).

With more advanced models of the Earth's density distribution, based, for example, on seismic tomography and crustal compilations, one can try to reproduce the observed gravity field by forward calculation. The more real Earth's density model is used, the better match with the observed field might be achieved. So far, such direct global budgeting was limited because models were provided either for limited depths (e.g., crust, lithosphere), or with a low resolution resembling the longest wavelengths of the geoid, or for well-surveyed regions only (e.g., Europe, North America), or they were provided in terms of seismic velocities only. Although with a partial Earth's density model the calculated gravity signal is necessarily incomplete, models that go significantly beneath the lithosphere bring little more because these masses participate in the hydrostatic equilibrium up to a certain extent. In gravity, this is manifested by large signal variations of individual Earth's layers like the crust compared with the observed anomalous field (Tenzer et al. 2012); a difference might reach a few orders of magnitude depending on the wavelength. Precisely this difference makes it possible to decipher basic spectral relations between large parts of the Earth even with an incomplete (depth-limited) density model.

In this paper, we study how the masses of the outermost 435 km of the Earth contribute to the gravitational anomalous field, how they contribute to the hydrostatic equilibrium on a global scale, and how the gravitational fields of these Earth layers are related with each other spectrally. The increasing spatial resolution and accuracy of density distribution models offer the opportunity to compare these data with satellite gravimetry. Relating Earth's structure models with totally independent satellite information can constrain knowledge of the Earth's crust and upper mantle. Note that isostatic adjustments of the LITHO1.0 gravity signal are intentionally avoided to see the immediate output of the model and to constrain such adjustments at the later stage. An overview of recent seismic tomography and lithospheric models is provided by Steinberger and Becker (2016). In our study, we have chosen the model LITHO1.0 (Pasyanos et al. 2014) because it provides a density variation to the depth of 435 km (below the lithosphere in most places) with a ~ 1 arc-deg resolution. LITHO1.0 incorporates CRUST1.0 (Laske et al. 2013) that makes the model more suitable for a direct comparison with satellite gravimetry; models like SAVANI (Auer et al. 2014) or GyPSuM (Simmons et al. 2010) use older CRUST2.0. Last but not least, our aim is to analyze how the gravitational gradients (Bouman et al. 2015, 2016) recently obtained by the ESA's mission GOCE (Flöberghagen et al. 2011) can globally be used with density models such as LITHO1.0. Unlike the geoid (and gravity),

the gradients are more sensitive to shallower density contrasts and they are thus less affected by deeper sources. Note that all calculations are done with absolute densities.

Section 1 introduces the input data used, i.e., the models LITHO1.0 and GOCO05s, and the numerical approach for converting densities in LITHO1.0 to the gravitational signal. With help from Appendix 1 the nodal parameterization of LITHO1.0 is discussed in detail. Section 2 provides gravity spectra of major (groups of) layers of the uppermost 435 km; this is done up to spherical harmonic degree 180 that corresponds with LITHO1.0's spatial resolution. This section also shows why density models like LITHO1.0 offer a useful laboratory for testing various density-related corrections to approach the observed gravity field—this is demonstrated by replacing a constant density of the mantle lid by the value obtained from LITHO1.0's primary wave and the velocity–density relation. Finally, Sect. 3 builds a complete synthetic Earth's gravitational field using LITHO1.0 (0–435 km) and ak135 (< 435 km) and compares the outcome with satellite gravimetry in terms of gravity vector and tensor components. For the sake of the related discussion, Appendix 2 gives a comparison of 1D and 3D integration applied to LITHO1.0's density columns.

2 Data and Processing

To represent the true gravitational field, we use the satellite-only model GOCO05s (Mayer-Guerr 2015), which is provided as a spherical harmonic expansion to degree and order 280. Up to degree 120 (165 km) GOCO05s benefits mainly from the GRACE mission (Tapley et al. 2004) and orbit tracking of low-orbit satellites while the higher degrees (> 120) rely on the GOCE mission (Mayer-Guerr 2015). The total error of gravity anomalies containing GOCE data such as GOCO05s is < 1 mGal at the resolution of 110 km (degree 180) (Meijde et al. 2015; Gruber 2015). This is by far superior to the accuracy of the gravitational signal calculated from any global Earth's density model available.

The upper Earth density structure is here represented by the LITHO1.0 model (Pasyanos et al. 2014), which is built upon the crustal model and seismic information. This model was constructed in order to fit high-resolution (Love and Rayleigh) surface wave dispersion maps. As prior information LITHO1.0 has used CRUST1.0 (Laske et al. 2013) for the crust and LLNL-G3D for the upper mantle (Simmons et al. 2012). LITHO1.0 consists of 40,962 nodes and 81,920 triangles within 154 layers. Each node has its own number of layers equipped with the primary and secondary seismic velocity, volumetric mass density, thickness (in terms of two radii R_1, R_2) and other parameters. Out of 154 layers the lowermost ones (1–127) come from the mean spherical 1D Earth model ak135 (Kennett et al. 1995) so that these might be evaluated as spherical shells. LITHO1.0 provides densities in the outer 435 kilometers of the Earth with respect to a mean radius 6371 km.

Important for the gravitational field is that LITHO1.0 provides a global density distribution down to the upper mantle. The upper and the lower part of the LITHO1.0 model are expected to be anti-correlated because the masses there participate, although it is not exactly known up to what extent, in a hydrostatic balance. Evaluating and summing individual layers thus provides their spectral relations directly.

Figure 1 provides the analysis of LITHO1.0 with respect to the radius (in green) and the mean thickness (in black) for all non-homogeneous layers (all that differ from a spherical shell either in density or in shape). As seen, the asthenosphere and the mantle lid are the thickest layers. From this figure, we can also anticipate why 1D Earth models and constant-

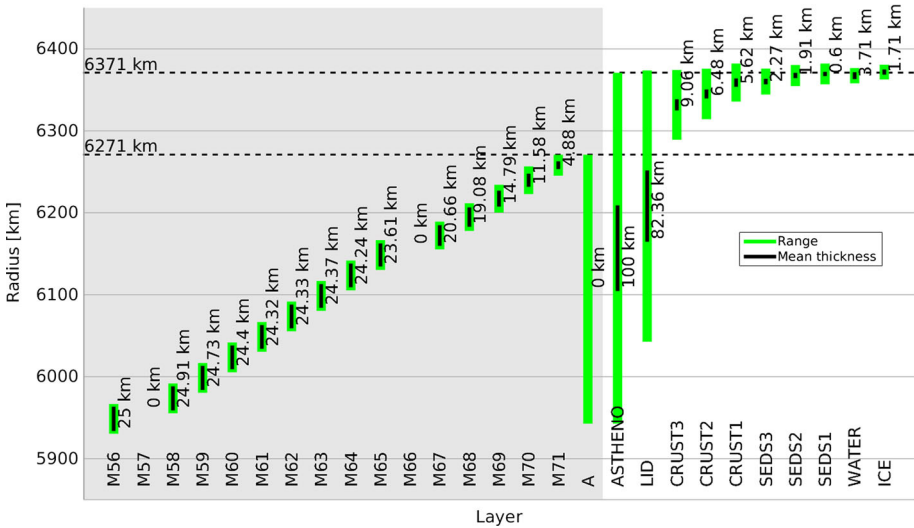


Fig. 1 The LITHO1.0 non-homogeneous layers in terms of the mean thickness (black) and the radial range (green). White and gray shading indicate two largest groups of layers involved in the gravitational equilibrium

depth approaches are insufficient for global geodynamic analyses. One average value for any given depth can hardly be used to represent the site-specific physical environment. The depths of Moho and Lithosphere-Asthenosphere boundary (LAB) of LITHO1.0 vary within [3, 76.3] and [58.4, 322] km (with respect to 6371 km), respectively. The LITHO1.0’s crustal thickness comes from balancing the prior model (CRUST1.0) and wave dispersion maps, whereas some artifacts were found over the oceans (Pasyanos et al. 2014, p. 2161). The model’s lithospheric thickness complies with the seismic definition (Artemieva 2006). Finally, note that LITHO1.0 contains also layers of zero thickness (M57, M66, A) that do not contribute to the gravitational signal, but indicate seismic discontinuities. For more information, see (Pasyanos et al. 2014, Table 1), which provides an overview of the uppermost layers with respect to prior information used in LITHO1.0.

2.1 Numerical Integration

To obtain the gravitational signal from a density distribution, it is straightforward to employ Green’s functions (Martinec 2014):

$$\begin{pmatrix} g_x \\ g_y \\ g_z \end{pmatrix}_{TRF} = -G \iiint_{x',y',z'} \frac{\rho(x',y',z')}{L^3} \begin{pmatrix} x-x' \\ y-y' \\ z-z' \end{pmatrix} dx'dy'dz', \tag{1}$$

where $L = \sqrt{(x-x')^2 + (y-y')^2 + (z-z')^2}$ and $G = 6.67408 \times 10^{-11} \text{kg}^{-1} \text{m}^3 \text{s}^{-2}$ are the gravitational constants and the product $dx'dy'dz'$ defines an infinitesimal volume element. Using the densities from LITHO1.0 and volume elements for each, the integral can be approximated with a sum over all layers and nodes:

$$\mathbf{g} = \begin{pmatrix} g_x \\ g_y \\ g_z \end{pmatrix}_{\text{TRF}} = -G \sum_{i=1}^N \sum_{j=1}^{n_i} \frac{\rho_{ij}(x', y', z')}{L^3} \begin{pmatrix} x - x'_{ij} \\ y - y'_{ij} \\ z - z'_{ij} \end{pmatrix} dV'_{ij}. \tag{2}$$

Similarly, the gravitational gradients can be calculated:

$$\mathbf{g}\mathbf{g} = \begin{pmatrix} g_{xx} & g_{xy} & g_{xz} \\ g_{xy} & g_{yy} & g_{yz} \\ g_{xz} & g_{yz} & g_{zz} \end{pmatrix}_{\text{TRF}} = \sum_{i=1}^N \sum_{j=1}^{n_i} \frac{-G\rho_{ij}}{L^5} \begin{pmatrix} L^2 - 3(x-x')^2 & -\frac{3(x-x')}{(y-y')^{-1}} & -\frac{3(x-x')}{(z-z')^{-1}} \\ -\frac{3(x-x')}{(y-y')^{-1}} & L^2 - 3(y-y')^2 & -\frac{3(y-y')}{(z-z')^{-1}} \\ -\frac{3(x-x')}{(z-z')^{-1}} & -\frac{3(y-y')}{(z-z')^{-1}} & L^2 - 3(z-z')^2 \end{pmatrix} dV'_{ij}. \tag{3}$$

The symbol dV'_{ij} denotes a volume element for each node as detailed in Appendix 1), N is the number of layers involved in the integration and n_i is the number of nodes used in each layer. The acronym TRF abbreviates the Terrestrial Reference Frame, in which the Cartesian axes point to the geocenter, whereas the xy plane lies in the equatorial plane (x pointing to the Greenwich meridian) and the z -axis is pointing to the North pole. The acceleration vector and the second-order tensor in the local tangential coordinate system are provided by Euler rotation (Arfken and Weber 2005):

$$\mathbf{g}_{\text{NWU}} = \mathbf{R}\mathbf{g}_{\text{TRF}}, \mathbf{g}\mathbf{g}_{\text{NWU}} = \mathbf{R}\mathbf{g}\mathbf{g}_{\text{TRF}}\mathbf{R}^\top \tag{4}$$

where the matrix $\mathbf{R}(\lambda, \theta)$ rotates the vector/tensor from the TRF to the North-West-Up (NWU) system and the elements of \mathbf{R} depend on the geocentric latitude and longitude only. The magnitude of the gravitational (acceleration) vector ℓ^2 -norm ($g = |\mathbf{g}|$) is invariant as well as the trace of $\mathbf{g}\mathbf{g}$ that must be zero in source-free space (Laplace’s equation).

To implement Eqs. (2 and 3) with LITHO1.0 is straightforward. The essential difference between Eqs. (1) and (2) is that the coordinates $\{x', y', z'\}$ in the latter refer to a volume and not to a point. Thus, for kernel calculations the volume element is referred to a mid-point along the geocentric radius for each layer $R_p(x', y', z') = (R_2 + R_1)/2$ with R_2 and R_1 being the upper and the lower layer boundary, respectively.

2.2 Validation and the Gravitational Signal

To demonstrate that Eqs. (2 and 3) are correctly used with LITHO1.0, the top panels of Fig. 2 show two distinct cases. Panel A examines the spherical shell of the uppermost constant-density layer in LITHO1.0 (called M55) at the radius of 6621 km. The shell theorem gives analytically $g_U = 6589$ mGal while panel A matches well this value with a variation 6590–6591 mGal. A small bias 0.5 mGal accounts for the 3D kernel employing R_p and non-zero g_N, g_W (with 0.2–0.3 mGal RMS). The triangular patterns in panel A well coincide with LITHO1.0 tessellation levels since the nodal densities cannot be equipped with surface/volume elements uniquely; see the discussion in Appendix 1. Using R_p the

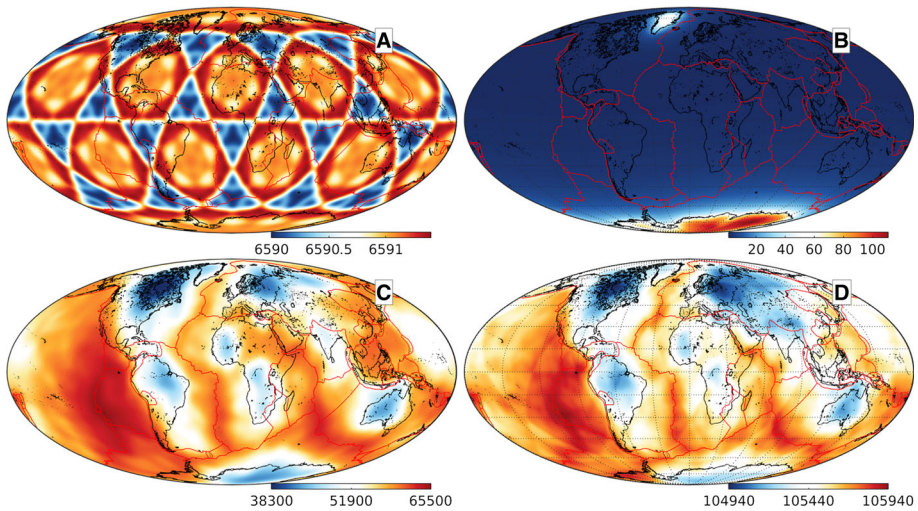


Fig. 2 Examples of the gravitational field calculated from LITHO1.0 on the sphere $r = 6621$ km. Panel A shows $|g|$ when the adopted integration scheme is applied to the shell-like layer M55, panel B shows the same quantity for the mean ice, panel C shows $|g|$ for the upper mantle (excluding the asthenosphere because of Fig. 1), while panel D shows the g_U (NWU) obtained with all non-homogeneous layers in LITHO1.0. Plate boundaries come from Bird (2003). Units are in mGal ($1 \text{ mGal} = 10^5 \text{ m/s}^2$)

integration error can be further decreased by additional vertical stratification. Unlike the lateral interpolation, this refinement does not modify LITHO1.0. Therefore, the original 27 non-homogeneous layers of the LITHO1.0 model were split into 145 layers. Each layer out of 27 was split into five except the mantle lid and the asthenosphere that were split into 10 layers. Panel B in Fig. 2 displays $|g|$ for the Earth's mean ice sheet although there is no exact formula to validate this result. The magnitudes and the spatial distribution are nonetheless realistic and correspond with other authors, e.g., see (Tenzer et al. 2015, Fig. 1). Overall, the adopted integration approach provides a reliable outcome and about 2–3 significant digits in the spatial domain. Of course, the numerical accuracy depends also on the distance from mass elements and on the wavelength. Numerical values for the quantities discussed are provided in Table 1.

Panel C in Fig. 2 shows $|g|$ for the upper mantle (the gray-shaded layers from Fig. 1) with a variation of about 27,150 mGal. Panel D shows g_U obtained from the whole LITHO1.0 model that will be used for the spectral analysis. From Table 1 and panels C, D it follows that the variation decreased to 1000 from 27,150 mGal; this is about 3.6%. Hence, LITHO1.0 within its 435 km represents a significant part of the Earth's (near-) hydrostatic equilibrium. The observed gravity signal variation, in turn, calculated with GOCO05s gives about 0.5% out of the upper mantle variation; see Table 1. Less than one order of magnitude is needed to approach the observed field. On the one hand, the discrepancy is caused by the errors in LITHO1.0 and by the numerical accuracy. On the other hand, the decrease to 3.6% only is also caused by a missing signal from below LITHO1.0 (manifested as a larger departure of LITHO1.0 from GOCO05s over long wavelengths in Fig. 3). It is known that long-wavelength geoid is generated in the mantle (Hager et al. 1985). This includes missing density information between TZ410 and TZ660 where seismic profiles show that velocity anomalies from above and from below ≈ 400 km might

Table 1 Basic numerical values for the results discussed in this article

Quantity	Min	Mean	Max	RMS	Note
$ g $	6590.0	6590.9	6591.4	6590.9	Fig. 2a
$ g $	1.3	16	156	35	Fig. 2b
$ g $	38,315	54,946	65,470	55,220	Fig. 2c
$g_U (\sim g)$	104,944	105,511	105,940	105,512	Fig. 2d
g_U	909,201	909,266	909,316	909,265	GOCO05s, d/o 180
g_U	- 26.6	0.06	34.4	8.4	Fig. 4 right
g_U	- 242/- 350	184/- 116	727/274	265/155	Fig. 5 left/ right
gg_{NN}	- 4.2	0.2	3.4	0.87	Fig. 6
gg_{NW}	- 1.9	0	2.7	0.45	Fig. 6
gg_{WW}	- 5.4	0.1	2.8	0.86	Fig. 6
gg_{NU}	- 5.8	- 0.03	4.3	1.0	Fig. 6
gg_{UU}	- 5.8	- 0.3	8.7	1.5	Fig. 6
gg_{WU}	- 3.9	0	6.0	1.0	Fig. 6

Quantities obtained from g and gg are in mGal ($1\text{ mGal} = 10^{-5} \text{ m/s}^2$) and in eotvos unit ($1\text{ EU} = 10^{-9} \text{ 1/s}^2$), respectively

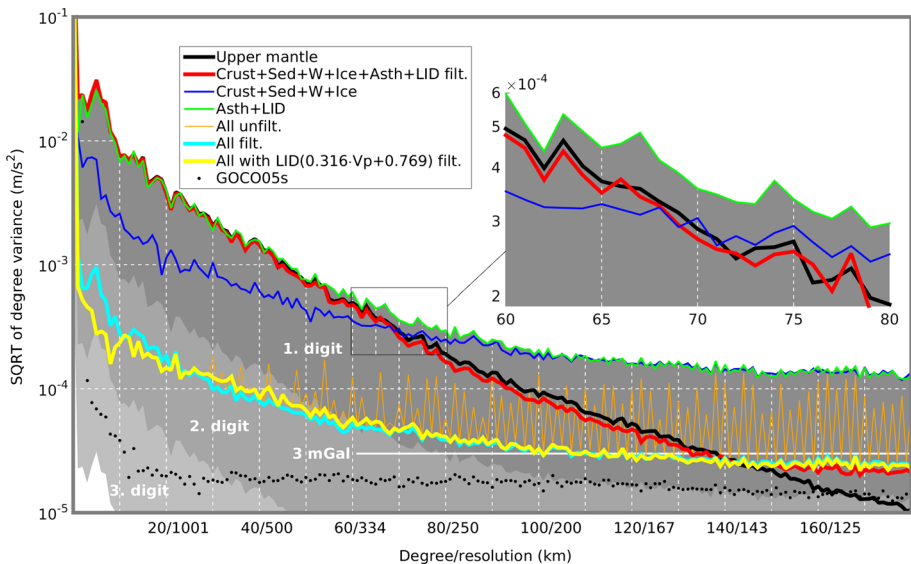


Fig. 3 Gravitational spectra—budget—of the upper Earth estimated at the ground level ($R = 6378.1363 \text{ km}$) with LITHO1.0 layers and compared with the satellite gravimetry model GOCO05s, in m/s^2 . “All” stands for the whole model LITHO1.0

be related and continuous tens of km below TZ410, e.g., see (Nolet et al. 2007, Fig. 2), (Li and Van Der Hilst 2010, Fig. 6) or (Fukao and Obayashi 2013, Fig. 3).

From panel D, we can see that local extremes are located over the tectonothermal young (and warm) and old (and cold) areas of the Earth. Panels A and D also partially

demonstrate the loss of significant digits as the icosahedron patterns occur at the second significant digits (see the Pacific ocean and compare with Fig. 7). Summing the gravitational effects of masses involved in the near-equilibrium state therefore directly validates the numerical integration. Panel D also shows that the whole LITHO1.0 model represents about 11% out of the total gravitational acceleration excluding the flattening.

3 Gravitational Budget of the Uppermost Earth

In Fig. 2 the colorbars for panels C and D indicate that the (direct) gravitational budgeting of the major uppermost Earth masses is necessarily limited by the accuracy of each layer and by missing data below LITHO1.0. As said above, the spectral relations between different layers might be valid as long as the variation of a total sum is (significantly) smaller than the variation of individual layers that are being summed. This is because the more Earth layers we evaluate, the better agreement with a relatively small variation of the observed anomalous field may be expected.

The gravitational field of the crust and the lithosphere is studied both locally and globally; e.g., see Ebbing et al. (2007), Fullea et al. (2015), Kaban et al. (2003), Kaban et al. (2010), Ebbing et al. (2013), Panet et al. (2014), Tenzer et al. (2009), Tenzer et al. (2015) and Bouman et al. (2015). However, the coupling between the layers (regions) on a global scale is not well known from a direct evaluation since the density structure for the crust and for the upper mantle was not provided in a consistent way as done by the LITHO1.0 model. Based on Fig. 1 we first group LITHO1.0 layers into two parts that couple most. These groups involve the asthenosphere with the whole lithosphere on one side and the upper mantle on the other side.

To obtain the spectrum for a given layer or a group of layers, Eqs. (2–4) are used to calculate particular vector and tensor quantities in the North-West-Up system. Then the Gauss–Legendre quadrature (Hildebrand 1987) is applied to g_U to obtain spherical harmonic coefficients. The quantity g_U in spherical harmonics reads

$$g_U = -\frac{GM}{R^2} \sum_{n=0}^{270} \sum_{m=0}^n (n+1) \left(\frac{R}{r}\right)^{n+2} (\bar{C}_{n,m} \cos m\lambda + \bar{S}_{n,m} \sin m\lambda) \bar{P}_{n,m}(\cos \theta), \quad (5)$$

where GM ($3.986004415 \cdot 10^{14} \text{ m}^3/\text{s}^2$) denotes the geocentric gravitational constant, $R = a_{\text{GOCO05s}} = 6,378,136.3 \text{ m}$ is the semimajor axis of the reference body, (r, θ, λ) is the set of geocentric coordinates, and $\bar{P}_{n,m}(\cos \theta)$ is the fully normalized associated Legendre function of the 1st kind. The maximum degree 270 of the coefficients $\bar{C}_{n,m}^s, \bar{S}_{n,m}^s$ corresponds to a number of latitudes in the grid entering the quadrature (271×540 points). Although LITHO1.0 lateral resolution is about 1 arc-deg degree, we evaluate Eqs. (2–3) on the target grid with a slightly higher resolution. This prevents a spectral leakage affecting the highest frequencies of the expansion. The altitude of the calculation was chosen to be close to the orbital altitude of GOCE, i.e., 250 km above 6,371 km. Although there is no exact relation between the tessellation level of a density model and the maximum spherical harmonic degree of the generated gravity signal, harmonic spectra are plotted up to degree 180 that gives a 1 arc-deg resolution on the sphere. The power spectral density (PSD) is provided in terms of the “degree variance” (Kaula 2000).

$$\text{PSD}(g_U)_n = \left(\frac{GM}{R^2}\right)^2 \sum_{m=0}^n (n+1)^2 \left(\frac{R}{r}\right)^{2n+4} (\bar{C}_{n,m}^2 + \bar{S}_{n,m}^2). \quad (6)$$

Before interpretations we shortly stray to the numerical errors. As seen from Figs. 2 and Appendix 1 a choice of the surface element leads to triangular artifacts in the resulting gravitational signal. Although the effect was significantly reduced from the first to second/third significant digit by using surface elements according to Appendix 1, it still enters the spherical harmonic analysis and may bias the spectra estimates (especially at higher frequencies).

In Fig. 3 the orange line shows the gravitational spectrum of g_U obtained from panel D in Fig. 2 (the whole LITHO1.0 model); see also Table 1 for the statistics. From degree 30 there is an apparent, strong and irregular oscillation that biases a realistic estimate of the PSD. Fig. 4 explains its nature in detail; on the left there are individual harmonic coefficients with $\bar{C}_{n,m}$ in the lower and $\bar{S}_{n,m}$ in the upper triangle. We can see that some cosine coefficients are systematically larger (blue stripes) with respect to the order. These stripes are a spectral response to the triangular patterns from Fig. 2 and affect only the resonant orders $m = 0, 5, 10, \dots$. The order five is not a coincidence, but it is related to a number of dominant patterns along the parallel in the spatial domain. Appendix 1 and Fig. 2 show that there are 5 largest structures along the parallel in each hemisphere that cause the “formal” resonance. The situation is reminiscent of resonance problems in satellite orbit dynamics (Kaula 2000; Vallado and McClain 2001), in which particular resonant orders linked with longitudinal parameters such as the Earth’s rotation and the nodal rate are strongly affected. Here, the resonant-like effects occur in the cosine terms from degree 30; thus, the spectrum estimate can be corrected by leaving out these columns in Eq. (6). Of course, there might be multiple other ways to filter this effect out but this one is simple and sufficient for our purpose. In the right panel of Fig. 4, we see g_U produced by the filtered-out coefficients. Obviously, regular triangular patterns with the magnitude variation ± 30 mGal are generated; see also Table 1. The corrected PSD from the whole model LITHO1.0 used in the following discussions is plotted in Fig. 3 as a cyan or yellow line. The corrected spectrum (cyan) has no “zigzag” patterns anymore, follows the orange curve (LITHO1.0 unfiltered) at its minima, and it preserves the magnitude at the degrees not affected by the oscillation. Note the resonant-like effect was already present in the red line

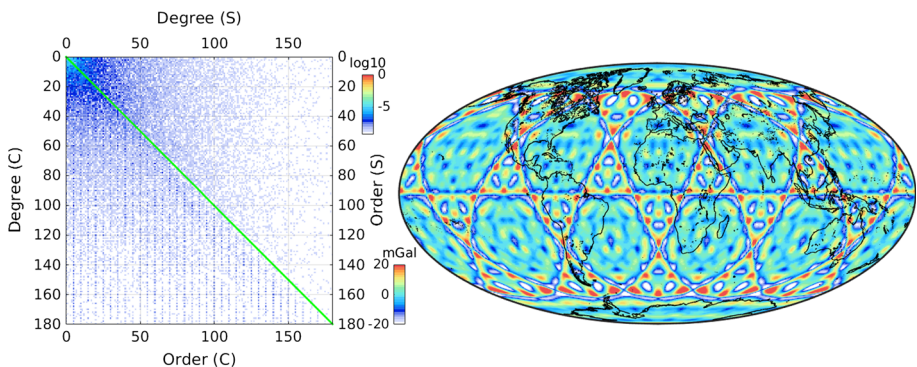


Fig. 4 A resonance-like effect in the harmonic analysis caused by the triangular icosahedron tessellation. The left panel shows the spherical harmonic coefficients of the LITHO1.0 gravitational signal (the orange curve in Fig. 3). The right panel shows g_U computed from resonant orders starting from degree 30

from degree 70—a sum of the gravitational effects from the asthenosphere and mantle lid (green) on one side, and, crust, sediments, ice and water on the other side. Again, as soon as some layers gravitationally couple, the numerical accuracy is questioned by summing their effects. With more complete and/or accurate Earth's density models, with which we get closer to the real gravity, the numerical issues associated with a model representation will become more pressing.

Compare now the corrected spectrum of the whole LITHO1.0 model (cyan) in Fig. 3 with the spectra generated by selected groups of layers. Note Fig. 3 shows the spectra up to degree 180 while the analysis was done to degree/order 270 to get rid of spectral leakage (a minor effect over largest degrees). The black dots represent the observed gravitational spectrum, which is used as a baseline, obtained from GOCO05s (Mayer-Guerr 2015), see Table 1 for statistics. From Fig. 3 we can see how large are individual contributors of the crust with sediments, ice and water (blue), the asthenosphere and the mantle lid (green), the upper mantle (black) compared with their sum (cyan). A significantly smaller power of the sum demonstrates how the hydrostatic balance is being manifested in the gravitational signal. The relatively small true anomalous gravitational field (± 150 mGal at the satellite altitude excluding the flattening) is being composed from very large contributions such as those from Fig. 3.

Compared to the upper mantle, the largest contribution in Fig. 3 (black solid line), it is seen that LITHO1.0 (cyan) provides more than one significant digit up to degree 60 (i.e., $< 10\%$) and slightly less over higher degrees. The nature of the interaction between the major layers significantly changes around degree 70. Up to this degree the interaction is driven by the asthenosphere+mantle lid (A + L, green) and the upper mantle (black). Then, from degree 70 onward the coupling is more driven by the A + L (green) and the crust, sediments, ice and water (blue). Around degree 110 the signal of the uppermost layers (blue) reaches the same magnitude as A + L (green). The remaining upper mantle (black) stops contributing significantly. While the upper mantle can be effectively eliminated by using degrees > 130 , Fig. 3 clearly shows that the role of the uppermost layers (crust, sediments, water, ice) is more peculiar. Hence for upper mantle studies, there is probably no cutoff spherical harmonic degree eliminating the crust from the analysis.

If the Earth's anomalous gravitational field would be solely caused by masses within the first 435 km, then the departure of LITHO1.0's signal from GOCO05s would simply equal the error of LITHO1.0 (GOCO05s error is negligible in this context). This is not the case since the data from below LITHO1.0 are not considered here (the remaining mantle and the core). It is known that especially the long-wavelength geoid is caused by deeper sources (Anderson 2007). Missing deep sources in our analysis explain why LITHO1.0 (cyan) departures from GOCO05s (black dots) more over long than short wavelengths. Over shorter wavelengths, a small contribution of the upper mantle from about degree 130 very likely means the cyan curve gets close to the LITHO1.0 error level – only A + L and crustal-like layers interact here. The spectrum becomes white from degree 110 roughly at the level of 3 mGal. Although this value is global, the LITHO1.0 model cannot be expected to have errors uniformly distributed in the vertical and lateral sense (Pasyanos et al. 2014, p. 2154)

Although any gravity field modeling is necessarily subject of non-uniqueness (e.g., the same signal can be created using different layers and different density variations), one can try to refine a particular Earth layer as long as the refinement seems to be more realistic than the status quo. For example, the total LITHO1.0 signal from Fig. 3 (cyan), which is based on panel D from Fig. 2, indicates that the total signal of LITHO1.0 significantly

departs from the observed field over the long wavelengths. As said above, this is mainly because of missing data from the mantle, but possibly also because the mantle lid in LITHO1.0 is equipped with a constant density. Pasyanos et al. (2014) explains that the constant value comes from the initial model. Based on Pasyanos (2017) we modified the density in the mantle lid by using a linear velocity–density relation $\rho = 0.316V_p + 0.769$ (with V_p in m/s and ρ in kg/m^3) from ACY400 (Montagner and Anderson 1989); e.g., recently used in Yegorova and Pavlenkova (2015), whereas the primary wave V_p is distributed along with LITHO1.0. Adding its gravitational signal to that from remaining LITHO1.0 layers, it results in the PSD represented by the yellow line from Fig. 3. The modification—a more realistic density variation in the mantle lid—significantly decreased the power over first ten degrees (up to 50%) toward the observed spectrum, while only a negligible change of the spectrum is seen beyond degree 90. This example basically shows why density models deep enough provide a useful platform for further geodynamic analyses – different geophysical scenarios (temperature, composition, etc.) can be tested while monitoring spectral relations between the layers. In addition, global evaluations like here avoid problems associated with the removal of long wavelengths with one cutoff frequency.

4 Anomalies from the Upper Earth Density Model and Satellite Gravimetry

Now the LITHO1.0 model will be combined with the remaining Earth’s layers taken from the ak135 model (Kennett et al. 1995) in order to obtain absolute gravitational discrepancies with the help from GOCO05s. The only necessary correction to compare LITHO1.0 and GOCO05s in the spatial domain accounts for the flattening. GOCO05s includes the flattening, but LITHO1.0 is a pure spherical Earth model without it. Because we do not want to lose connection with LITHO1.0, not the density model, but the observed field (GOCO05s) is reduced for the flattening. This is accomplished by reducing GOCO05s zonal harmonics $\bar{C}_{2,0}$, $\bar{C}_{4,0}$, $\bar{C}_{6,0}$, $\bar{C}_{8,0}$ for those from the GRS80 ellipsoid (Moritz 2000).

To obtain a (synthetic) full-earth gravitational signal, we add to LITHO1.0 a signal from ak135 model calculated from the shell formula (for $r > R_i$):

$$g_U = -\frac{4}{3}\pi G \sum_{i=1}^n \rho_i \frac{R_{i+1}^3 - R_i^3}{r^2}, \quad (7)$$

where r is a given radius, R_{i+1} and R_i is the upper and the lower radius of a particular spherical shell, respectively. The integer n denotes a number of shells involved. The LITHO1.0 model is already equipped with the densities from ak135 so that the use of both models together is straightforward.

The “absolute” discrepancies in terms of g_U , that correspond to the full LITHO1.0 signal (cyan in Fig. 3), are plotted in the left panel of Fig. 5 (see also Table 1). The magnitudes reach hundreds of mGal, but they are not randomly distributed. The largest values are located over cold (such as cratonic) and hot areas (such as oceanic ridges), while the lowest systematically depart from both thermal extremes (green-yellow boundaries in Fig. 5). Indeed, residuals such as in the left panel of Fig. 5 suggest to refine densities in some LITHO1.0 layer(s) that might be linked with thermal and composition effects. The blue histogram in Fig. 5 then shows how much the discrepancies are not centered.

As mentioned above, large discrepancies in Fig. 5 (left) coming from LITHO1.0 can be caused by $\rho = 3300 \text{ kg/m}^3$ used both for the mantle lid and the asthenosphere. Such a

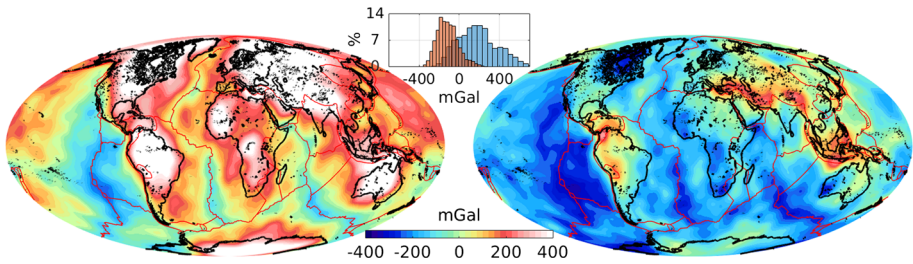


Fig. 5 Residual g_U signal from GOCO05s, LITHO1.0 (cyan curve in Fig. 3) and ak135 obtained at the altitude of 250 km to degree 180, in mGal (10^{-5}m/s^2). Plate boundaries based on Bird (2003)

constant value is not realistic especially for the mantle lid because its density is known to be dependent on the temperature and composition (e.g., Afonso et al. (2016)) which correlates with the tectonothermal age. For example, Zoback and Mooney (2003) uses $\rho = 3320 - 3340 \text{ kg/m}^3$ for masses above the asthenosphere. As explained in Pasyanos et al. (2014) $\rho = 3300 \text{ kg/m}^3$ was not changed during the iteration when fitting wave dispersion maps. Note Fig. 5 (left) interestingly matches the thermal correction to V_s in Simmons et al. (2010, Fig. 6) and the temperature-induced gravity anomaly in Kaban et al. (2003, Fig. 9).

In the previous section, the velocity–density relation was employed to modify the density of the mantle lid while the spectrum to degree 10 (yellow line) became significantly closer to the observed spectrum. The right panel of Fig. 5 shows g_U computed from the same coefficients as used for the modified LITHO1.0 spectrum (yellow line in Fig. 3). It is seen the residuals substantially changed over the globe, especially in the areas where LITHO1.0's mantle lid is very thick (the white areas in Fig. 5). The red histogram in Fig. 5 shows that the residuals are again off center but on the opposite side than before. The residuals are now more concentrated around the main bin. The RMS values from Table 1 for both panels in Fig. 5 quantify the difference between the unmodified (cyan) and the modified (yellow) coefficients—the RMS decreased from 265 to 155 mGal. Dominant patterns in the right panel of Fig. 5 resemble the structures that do not seem to be associated with the mantle lid or the layers above the mantle lid. Most likely, these residuals come from deeper areas and thus they possibly highlight other areas for further refinement. Of course, there is the ubiquitous problem of non-uniqueness—but this can be prevented only by omitting gravity data at all. The main lesson here is that with density models deep enough to contain masses participating, to a certain extent, in the near-hydrostatic equilibrium, we are much closer to the observed field than with any lithosphere/asthenosphere model. Hence the sensitivity for density-related modifications is much higher than with the model of lithosphere/asthenosphere only (i.e., compare the relation of the red line from Fig. 3 with that of GOCO05s vs. the difference between the cyan and yellow line).

Finally, to better localize the sources of discrepancies shown in the right panel of Fig. 5 the same evaluation (LITHO1.0 and ak135 vs. GOCO05s) is provided in Fig. 6 in terms of the gravitational gradients. For example, compare g_U from Fig. 5 (right) with its radial derivative gg_{UU} . We see that the discrepancies are more concentrated in the neighborhood of subduction zones (red) and over the oceanic ridges (blue). Obviously, the width/sensitivity of the kernel function enters the geophysical interpretation. Other diagonal components gg_{NN}, gg_{WW} from Fig. 6 systematically highlight the same areas but in a given direction (this comes from Laplace's equation $gg_{NN} + gg_{WW} = -gg_{UU}$). The remaining gradients may highlight places not well indicated by the diagonal components. For example, gg_{NU} is large (in its absolute value) in the Arabian peninsula or the Central America.

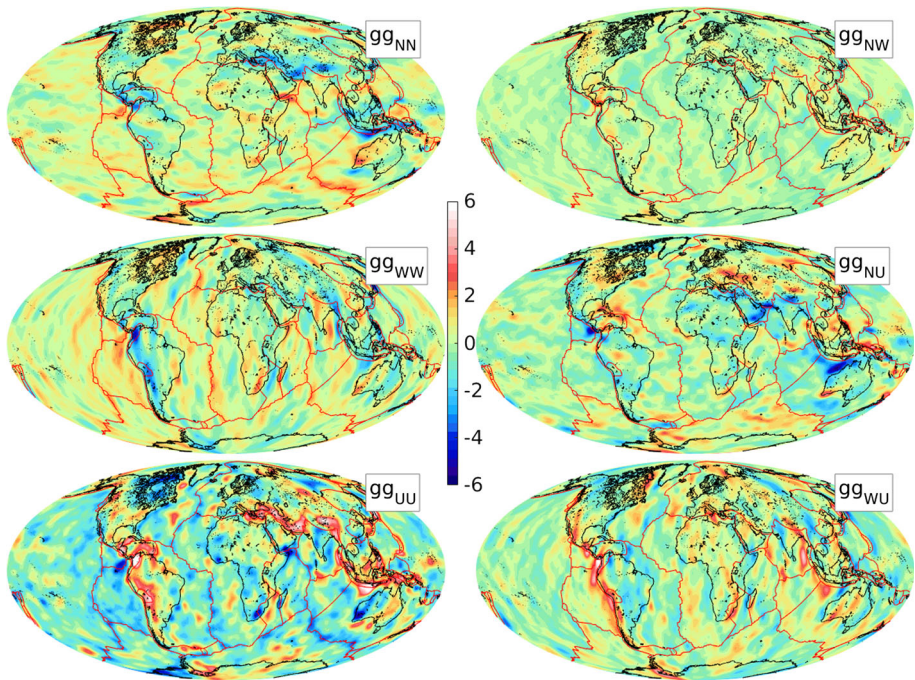


Fig. 6 Residual gravitational gradients from GOCO05s, LITHO1.0 (yellow curve in Fig. 3) and ak135 obtained at the altitude of 250 km to degree 180, in eotvos (10^{-9}s^{-2}). Plate boundaries based on Bird (2003)

5 Summary and Conclusions

This paper evaluates the gravitational field of the density model for the outermost 435 km of the Earth. Large gravitational signal variations of individual layers substantially decrease toward the observed field in the sum (see Figs. 2, 3)—a manifestation of masses participating in the near-hydrostatic equilibrium in terms of the gravitational signal. The deeper and more realistic is the density model the better should the match with the observed field be—in this case global spectra like those in Fig. 3 will approach the observed field. Satellite gravimetry nowadays gives a very accurate reference at a higher resolution than that of global density distribution models available.

The spectral budget in Fig. 3 gives a clue to a use of lithospheric and upper mantle models in gravity-related geodynamics. Although LITHO1.0 errors and missing masses below bias the estimated spectra, the total signal of 435 km of mass (cyan and yellow lines in Fig. 3) is significantly lower than the signal of all the main layers involved. The estimated spectra are thus valid with the uncertainty of about 5–10% depending on the wavelength. Figure 3 therefore allows us to distinguish two important spectral zones. At degrees > 130 the upper mantle gradually stops contributing, while its error must be small since it does not contribute much and only with a first significant digit. The gravitational field is here driven solely by the relation of the uppermost layers (crust, sediments, etc.) and the asthenosphere/mantle lid (A + L). Moreover, the total LITHO1.0 spectrum (cyan or yellow in Fig. 3) over higher degrees becomes flat near the 3 mGal level that is plausibly close to the accuracy of LITHO1.0 (assuming the missing mantle does not add much)

and provides an input for the isostatic adjustment within the lithosphere. For these degrees (> 130) especially ESA's gradiometry mission GOCE supports global analyses with high-accuracy gravitational gradients. Below degrees 110–130 the situation in the uppermost Earth is more complicated. Although low wavelengths are governed by the A + L and the upper mantle layers, the role of the crust is not negligible over all wavelengths (blue curve in Fig. 3). The quality of the crustal density models over long wavelengths is thus crucial for accessing deeper areas with gravity data. The crustal field starts to dominate over the upper mantle around degree 70 although this value may slightly change by considering densities below 435 km. Overall, A + L from Fig. 3 (green line) is shown to play a role of a “double-agent”—it produces largest magnitudes over all wavelengths while interacting with the upper mantle over long and with the crust over shorter wavelengths.

The model ak135 below 435 km was added to LITHO1.0 to obtain absolute discrepancies by comparing it with the observed field (GOCO05s). For the mantle lid we have tested two options. In the first the original density from LITHO1.0 was used (constant value for the whole layer) while in the second one the density was obtained from the primary wave V_p and the velocity–density relation. While the first option (Fig. 5 left) shows large discrepancies over hot (oceanic ridges) and cold areas (e.g., cratons) resembling a temperature-driven density variation [see Simmons et al. 2010, Fig. 6 and Kaban et al. 2003, Fig. 9)], the velocity–density relation dramatically reduced the discrepancy for about 40% in terms of RMS (see Fig. 5 right and Table 1). The second option thus seems to resolve the large misfit due to the mantle lid and allows us to continue making further refinements. The velocity–density relation affected namely the spectrum over first degrees; see Fig. 3. For a more detailed look at the misfit between LITHO1.0 (with modified mantle lid), ak135f and GOCO05s Fig. 6 shows the gravitational gradients in the spatial domain. Especially diagonal components (e.g., gg_{UU}) show that the misfit is related to masses beneath the mantle lid since the major patterns do not correlate with the density/thickness of this layer—both radial components from Figs. 5 and 6 show the large values follow subduction zones.

The LITHO1.0 model was shown to be an appropriate global density distribution model useful for global geodynamic research. A more comprehensive study is possible because LITHO1.0 shares the same parameterization with the mantle model LLNL-G3Dv3 (Simmons et al. 2012). Although icosahedron parameterization used in LITHO1.0 suffers from an ambiguity when setting up volume elements (triangles vary in area and each may have three different densities), the problem can be overcome in the spectral domain because the effect produces very regular patterns with respect to the spherical harmonic order of the gravitational field expansion. For deeper areas in the mantle, this numerical issue will be less important since the effect naturally ceases with the depth.

Acknowledgements The study is connected to the ESA STSE project “3D Earth - A Dynamic Living Planet” (<https://www.3dearth.uni-kiel.de/en>). We thank the Editor in Chief Michael J. Rycroft and anonymous reviewers for their helpful comments.

Appendix 1: Choice of Volume Elements

Triangular parameterizations such as that used in LITHO1.0 are not often used for calculating the Earth's gravitational signal from a global density distribution; see, however, the exception (Haagmans 2000). The situation is complicated by the fact that each node might be equipped with a unique value of the density and individual triangles may differ in area. This causes an ambiguity in a way the volume element can be set up.

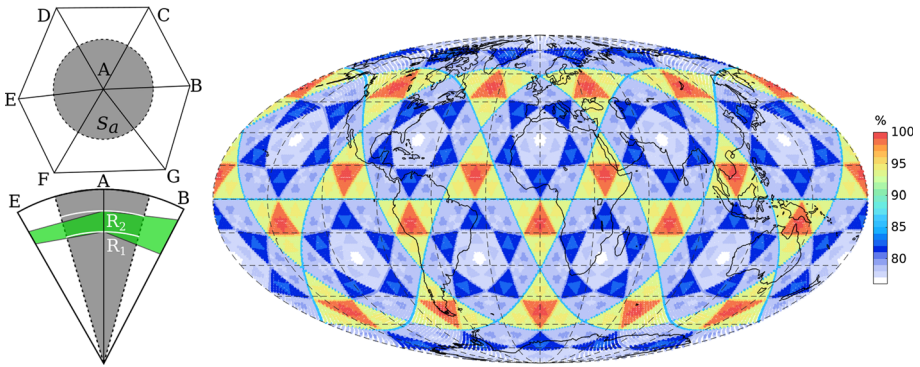


Fig. 7 On the left, the average solid angle of each node for setting up volume elements according to Eq. (8). On the right, the global variation of S_a in percent (relatively to the largest value) obtained from LITHO1.0

To reduce the effect of triangulation in LITHO1.0, we define the volume element of each node according to Fig. 7 as space between two spherical surfaces (R_1 and R_2) for a specific solid angle:

$$dV' = \frac{1}{3} S_a (R_2^3 - R_1^3), \quad (8)$$

where $R_1 \leq R_2$ and S_a is the average solid angle from the all spherical triangles containing the particular node. The gray area on the left of Fig. 7 depicts S_a , white radii bound the volume element vertically and the green area shows the discretized layer passing from node to node. Because the number of nodes is half of the number of triangles (40,962 nodes vs. 81,920 triangles), the local average S_a must be multiplied by two (or exactly by 81,920/40,962) to cover 4π . Nonetheless, a global sum of such average S_a will deviate from 4π . In our case, the error is $\delta = 4.4 \cdot 10^{-5}$ steradian that corresponds to more than 5 significant decimal digits of 4π . To compare, a sum of all spherical triangles provided with LITHO1.0 gives 4π with the error $\delta = -3.5 \cdot 10^{-10}$ steradian. Hence, the volume numerical integration with models like LITHO1.0 is a sort of a trade-off between a way the local average is made (to assign the density to a volume) and preservation of the whole Earth surface/mass.

The variation of the average surface elements in percent is shown on the right of Fig. 7. The patterns agree well with the process of tessellation used in LITHO1.0; nearly each tessellation level can be recognized (from large to small patterns). The area variation is computed with respect to the largest value (red) and it reaches up to 22%. For example, omitting this area variation and using a constant value for each node (i.e., $S_a = 4\pi/40962$) affects all significant digits of the resulting gravitational signal.

Appendix 2: Comparison of 1D and 3D Integration

One dimensional approximations such Eq. (7) are often being used to calculate the gravity signal from a density column ρ_i (Turcotte and Schubert 2002; Hees 2000). Although not by definition, the shell formula may also provide a quasi-lateral variation if each density column is evaluated separately. Hence, by using all the non-homogeneous layers in LITHO1.0 a 3D approach based on Eq. (4) can be confronted with Eq. (7).

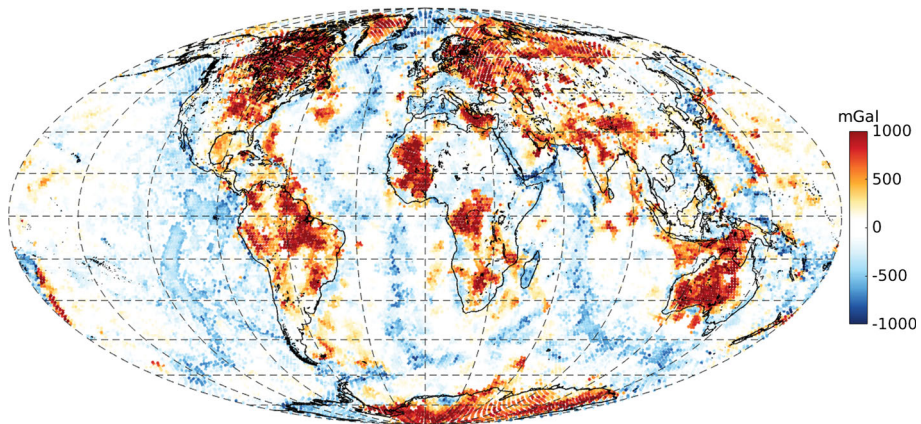


Fig. 8 A difference in g_U (in mGal) between Eqs. (2) and (7) at 6621 km by using all the non-homogeneous layers in LITHO1.0

Figure 8 shows such a difference in terms of g_U . It is seen the large discrepancies are located over the thick parts of the lithosphere and over the oceanic ridges where the shell formula simply does not account for a lateral density variation. The magnitudes reach ± 1000 mGal that is more than twice as much as the difference between GOCO05s and LITHO1.0 (including ak135) evaluated with Eq. (2); see Fig. 5 and Table 1. The 1D approximation would introduce a large methodological error in our context. On the other hand, Eq. (7) is not singular (compare with Eq. (2) when $L \rightarrow 0$) and it is much faster to evaluate than Eq. 2 (seconds vs. hours on a single PC).

References

- Afonso JC, Rawlinson N, Yang Y, Schutt DL, Jones AG, Fullea J, Griffin WL (2016) 3-D multiobservable probabilistic inversion for the compositional and thermal structure of the lithosphere and upper mantle: III. Thermochemical tomography in the Western-Central US. *J Geophys Res Solid Earth* 121(10):7337–7370
- Anderson DL (2007) *New theory of the earth*. Cambridge University Press, Cambridge
- Arfken GB, Weber HJ (2005) *Mathematical methods for physicists international student edition*. Academic press, Cambridge
- Artemieva IM (2006) Global 1×1 thermal model TC1 for the continental lithosphere: implications for lithosphere secular evolution. *Tectonophysics* 416(1):245–277
- Auer L, Boschi L, Becker T, Nissen-Meyer T, Giardini D (2014) Savani: a variable resolution whole-mantle model of anisotropic shear velocity variations based on multiple data sets. *J Geophys Res Solid Earth* 119(4):3006–3034
- Bertotti B, Farinella P, Vokrouhlicky D (2012) *Physics of the solar system: dynamics and evolution, space physics, and spacetime structure*, vol 293. Springer, Berlin
- Bird P (2003) An updated digital model of plate boundaries. *Geochem Geophys Geosyst* 4(3):
- Bouman J, Ebbing J, Meekees S, Fattah RA, Fuchs M, Gradmann S, Haagmans R, Lieb V, Schmidt M, Dettmering D et al (2015) GOCE gravity gradient data for lithospheric modeling. *Int J Appl Earth Obs Geoinf* 35:16–30
- Bouman J, Ebbing J, Fuchs M, Sebera J, Lieb V, Szwillus W, Haagmans R, Novak P (2016) Satellite gravity gradient grids for geophysics. *Sci Rep*. <https://doi.org/10.1038/srep21050>
- Chase CG (1979) Subduction, the geoid, and lower mantle convection. *Nature* 282:29

- Cubells, J., Calsamiglia, A. (2010). Transitando por los espacios jurídico-penales: Discursos sociales e implicaciones para la intervención en casos de violencia hacia la mujer. *Acciones e Investigaciones Sociales* 28, 79–108
- De Pater I, Lissauer JJ (2015) Planetary sciences. Cambridge University Press, Cambridge
- Denis C, Rogister Y, Amalvict M, Delire C, Denis AI, Munhoven G (1997) Hydrostatic flattening, core structure, and translational mode of the inner core. *Phys Earth Planet Inter* 99(3):195–206
- Ebbing J, Brautenberg C, Wienecke S (2007) Insights into the lithospheric structure and tectonic setting of the Barents Sea region from isostatic considerations. *Geophys J Int* 171(3):1390–1403. <https://doi.org/10.1111/j.1365-246X.2007.03602.x>
- Ebbing J, Bouman J, Fuchs M, Lieb V, Haagsmans R, Meekes J, Fattah RA (2013) Advancements in satellite gravity gradient data for crustal studies. *Lead Edge* 32(8):900–906
- Floberghagen R, Fehrer M, Lamarre D, Muzi D, Frommknecht B, Steiger C, Piñeiro J, Da Costa A (2011) Mission design, operation and exploitation of the gravity field and steady-state ocean circulation explorer mission. *J Geodesy* 85(11):749–758
- Fukao Y, Obayashi M (2013) Subducted slabs stagnant above, penetrating through, and trapped below the 660 km discontinuity. *J Geophys Res Solid Earth* 118(11):5920–5938
- Fullea J, Rodríguez-González J, Charco M, Martinec Z, Negredo A, Villaseñor A (2015) Perturbing effects of sub-lithospheric mass anomalies in GOCE gravity gradient and other gravity data modelling: application to the Atlantic-Mediterranean transition zone. *Int J Appl Earth Obs Geoinf* 35:54–69
- Gruber T (2015) GOCE gravity field models-signal and error assessment. In: EGU general assembly conference abstracts, vol 17, p 1657
- Haagsmans R (2000) A synthetic earth for use in geodesy. *J Geodesy* 74(7–8):503–511
- Hager BH, Clayton RW, Richards MA, Comer RP, Dziewonski AM (1985) Lower mantle heterogeneity, dynamic topography and the geoid. *Nature* 313:541–545. <https://doi.org/10.1038/313541a0>
- van Hees GS (2000) Some elementary relations between mass distributions inside the earth and the geoid and gravity field. *J Geodyn* 29(1):111–123
- Hildebrand FB (1987) Introduction to numerical analysis. Courier Corporation, North Chelmsford
- James R, Kopal Z (1962) The equilibrium figures of the earth and the major planets. *Icarus* 1(1–6):442–454
- Kaban M, Tesauro M, Cloetingh S (2010) An integrated gravity model for Europe’s crust and upper mantle. *Earth Planet Sci Lett* 296(3):195–209
- Kaban MK, Schwintzer P, Artemieva IM, Mooney WD (2003) Density of the continental roots: compositional and thermal contributions. *Earth Planet Sci Lett* 209(1):53–69
- Kaula WM (2000) Theory of satellite geodesy: applications of satellites to geodesy. Dover Publications, Mineola
- Kennett B, Engdahl E, Buland R (1995) Constraints on seismic velocities in the Earth from traveltimes. *Geophys J Int* 122(1):108–124
- Laske G, Masters G, Ma Z, Pasyanos M (2013) Update on CRUST1.0A 1-degree global model of Earth’s crust. *Geophys Res Abstr* 15:2658
- Li C, Van Der Hilst RD (2010) Structure of the upper mantle and transition zone beneath Southeast Asia from traveltimes tomography. *J Geophys Res Solid Earth* 115(B7):
- Martinec Z (2014) Mass-density Green’s functions for the gravitational gradient tensor at different heights. *Geophys J Int* 196(3):1455–1465
- Mayer-Guerr T (2015) The combined satellite gravity field model GOCO05s. In: EGU general assembly conference abstracts, vol 17, p 12364
- Montagner JP, Anderson DL (1989) Constrained reference mantle model. *Phys Earth Planet Inter* 58(2–3):205–227
- Moritz H (2000) Geodetic reference system 1980. *J Geodesy* 74(1):128–133
- Nolet G, Allen R, Zhao D (2007) Mantle plume tomography. *Chem Geol* 241(3):248–263
- Panet I, Pajot-Métivier G, Greff-Lefftz M, Métivier L, Diamant M, Mandea M (2014) Mapping the mass distribution of Earth’s mantle using satellite-derived gravity gradients. *Nat Geosci* 7(2):131–135
- Pasyanos M (2017) Personal communication
- Pasyanos ME, Masters TG, Laske G, Ma Z (2014) LITHO1.0: an updated crust and lithospheric model of the earth. *J Geophys Res Solid Earth* 119(3):2153–2173
- Simmons NA, Forte AM, Boschi L, Grand SP (2010) GyPSuM: a joint tomographic model of mantle density and seismic wave speeds. *J Geophys Res Solid Earth* 115(B12):
- Simmons NA, Myers SC, Johannesson G, Matzel E (2012) LLNL-G3Dv3: Global P wave tomography model for improved regional and teleseismic travel time prediction. *J Geophys Res Solid Earth* 117(B10):
- Steinberger B, Becker TW (2016) A comparison of lithospheric thickness models. *Tectonophysics*

- Tapley BD, Bettadpur S, Watkins M, Reigber C (2004) The gravity recovery and climate experiment: Mission overview and early results. *Geophys Res Lett* 31(9):
- Tenzer R, Hamayun K, Vajda P (2009) Global maps of the crust 2.0 crustal components stripped gravity disturbances. *J Geophys Res Solid Earth* 114(B5):b05408. <https://doi.org/10.1029/2008JB006016>
- Tenzer R, Novák P, Vajda P, Gladkikh V (2012) Spectral harmonic analysis and synthesis of Earth's crust gravity field. *Comput Geosci* 16(1):193–207
- Tenzer R, Chen W, Tsoulis D, Bagherbandi M, Sjöberg LE, Novák P, Jin S (2015) Analysis of the refined CRUST1.0 crustal model and its gravity field. *Surv Geophys* 36(1):139–165
- Turcotte D, Schubert G (2002) *Geodynamics*, 2nd edn. Cambridge University Press, New York
- van der Meijde M, Pail R, Bingham R, Floberghagen R (2015) GOCE data, models, and applications: a review. *Int J Appl Earth Obs Geoinf* 35:4–15
- Vallado D, McClain W (2001) *Fundamentals of astrodynamics and applications*, space technology library. Kluwer Academic Publishers, Dordrecht, p 792
- Yegorova T, Pavlenkova G (2015) Velocity-density models of the earth's crust and upper mantle from the quartz, craton, and kimberlite superlong seismic profiles. *Izvestiya Phys Solid Earth* 51(2):250
- Zoback ML, Mooney WD (2003) Lithospheric buoyancy and continental intraplate stresses. *Int Geol Rev* 45(2):95–118